MgF2-Based Organized Porous Inorganic Nanofluorides as Heterogeneous Catalysts for Fluorination of 2-Chloropyridine

Zahra Goharibajestani, Yawen Wang, Valentine Camus-Génot, Sandrine Arrii, Jean Dominique Comparot, Baptiste Polteau, Jérôme Lhoste, Cyrille Galven, Veyis Gunes, Annie Hémon-Ribaud, et al.

MgF2-Based Organized Porous Inorganic Nanofluorides as Heterogeneous Catalysts for Fluorination of 2-Chloropyridine

Sylvette Brunet, Zahra Goharibajestani, Yawen Wang, Valentine Camus-Génot, Sandrine Arrii, Jean Comparot, Baptiste Polteau, Jérôme Lhoste, Cyrille Galven, Veyis Gunes, et al.

MgF_2-Based Organized Porous Inorganic Nanofluorides as Heterogeneous Catalysts for Fluorination of 2-Chloropyridine

Zahra Goharibajestani, Yawen Wang, Valentine Camus-Genot, Sandrine Arrii, Jean Dominique Comparot, Baptiste Polteau, Jérôme Lhoste, Cyrille Galven, Veyis Gunes, Annie Hémon-Ribaud, Sagrario Pascual, Monique Body, Christophe Legein, Vincent Maisonneuve, Sylvette Brunet,* and Amandine Guiet*

Cite This: https://doi.org/10.1021/acsanm.1c01768

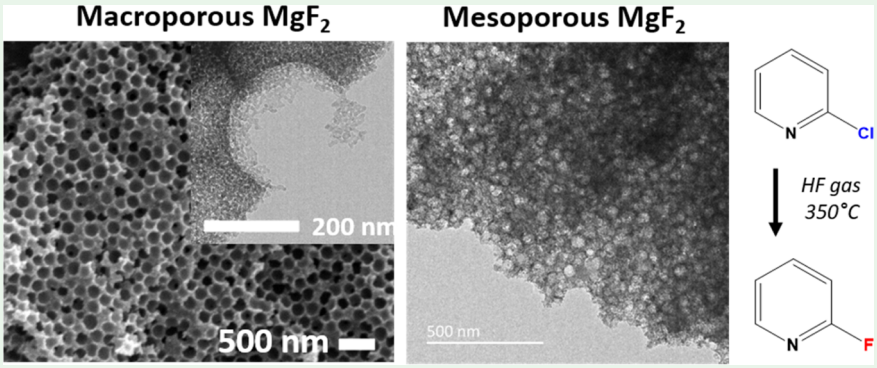

ABSTRACT: The successful preparation of organized porous inorganic fluorides (OPIFs) with a high specific surface area is demonstrated for MgF_2. For the first time, macroporous MgF_2 OPIFs with a surface area of above 200 $m^2 g^{-1}$ and mesoporous MgF_2 powder were prepared through the assembly of preformed MgF_2 nanoparticles and homemade polymer templates with a tunable size. These OPIF materials have been fully examined at different synthesis stages by means of powder X-ray diffraction, N_2 sorption, scanning electron microscopy, and transmission electron microscopy analyses and ^{19}F and ^{1}H solid-state nuclear magnetic resonance. The relation between the nature, the size, and the amount of polymer template on the porous structure was deeply investigated. The MgF_2 OPIFs present a higher thermal stability under air and F_2 calcination than MgF_2 NPs as the structuration of the OPIF composite considerably slows down the crystallite growth during thermal treatment under air. OPIF materials were evaluated for the first time as heterogeneous catalysts for the fluorination of 2-chloropyridine under HF gas as a fluorinating agent at 350 °C. This study evidences catalytic sites with two Lewis acidity strengths (medium and low).

KEYWORDS: *magnesium fluoride, organized porous inorganic fluorides (OPIFs), polymer template, nanoparticles, heterogeneous catalyst, HF gas fluorination, 2-chloropyridine*

1. INTRODUCTION

Owing to their outstanding characteristics such as a high specific surface area, tunable pore size and shape, various structures, and multiple compositions, three-dimensional (3D) porous inorganic materials have been used in various applications such as catalysis, adsorption sensors, lithium-ion batteries, drug delivery, and nanodevices.[1−3] Since the discovery of organized mesoporous silica in the early 1990s,[4] 3D porous inorganic materials have been extensively studied for metal oxides, metal sulfides, and carbons, and their synthesis relies on template-assisted methodologies including (i) the soft-templating method, (ii) the hard-templating method, and (iii) the colloid crystal templating (CCT) method[3,5] (Scheme S1). Briefly, the soft-templating method using surfactants or block copolymers as the template is mainly used for the preparation of mesoporous silica and mesoporous metal oxides.[3,5,6] This method is based on evaporation-induced self-assembly of the organic template with the inorganic precursors to form an ordered organic−inorganic composite. Template removal by calcination results in the mesoporous inorganic material. In the second template-assisted approach, known as hard-templating or nanocasting, ordered mesoporous

Received: July 22, 2021
Accepted: September 27, 2021

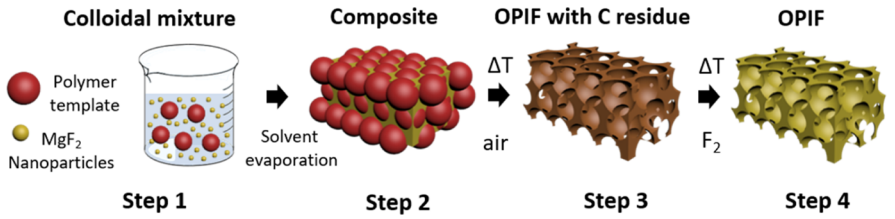

Figure 1. Schematic representation of the different steps of the MgF_2 OPIF synthesis.

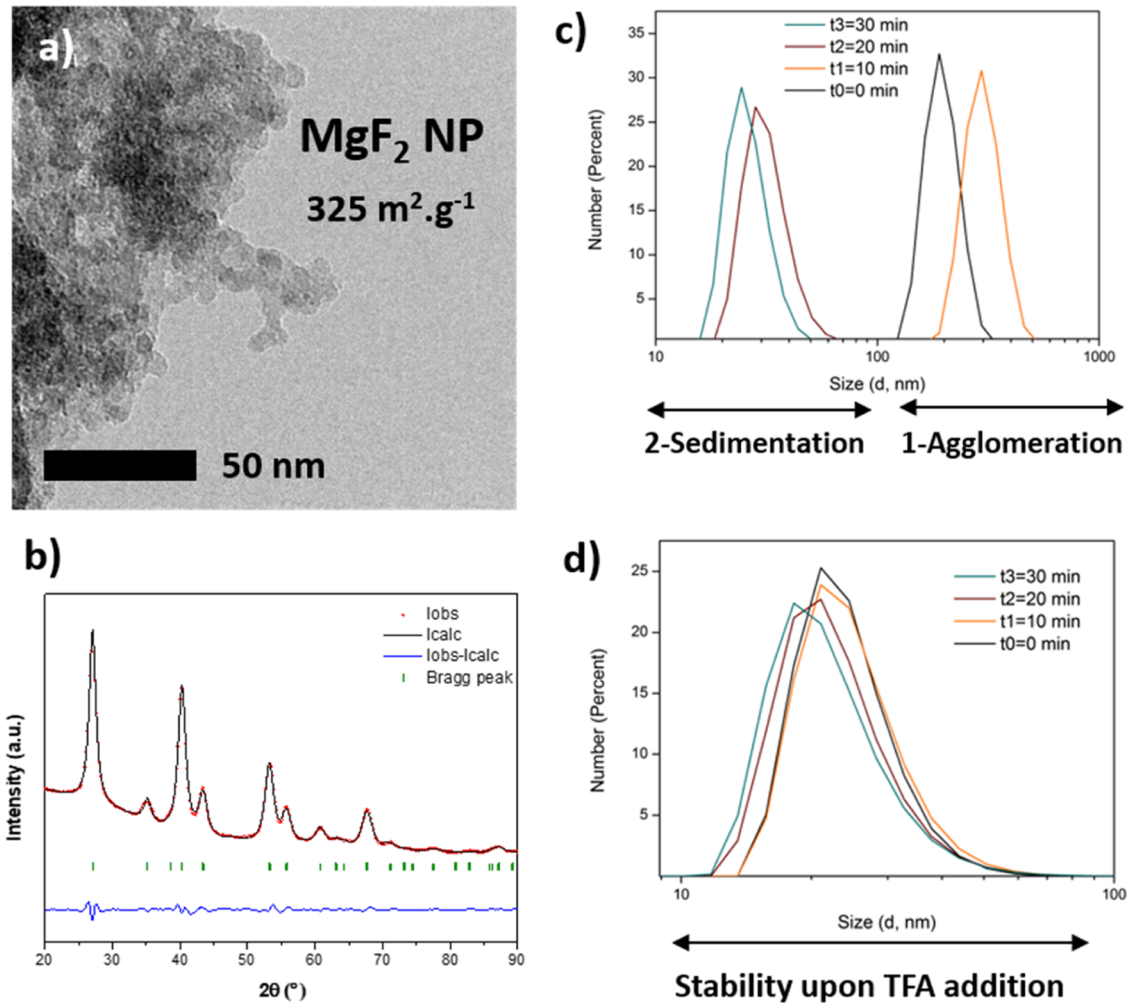

Figure 2. (a) TEM image of MgF_2 NPs. (b) Le Bail refinement of MgF_2 NPs. Vertical markers give the Bragg peak positions of the tetragonal space group $P4_2/mnm$ (no. 136). DLS of MgF_2 NPs dispersed in water with time (c) without TFA and (d) with TFA as the stabilizing agent.

silica (SBA-15 or MCM-41) or alumina is used as a mold by introducing metallic precursors into the pore channels.[7−10] The rigid template is chemically removed to obtain ordered nano-objects. The last approach, CCT strategy,[3,5] often mixed in the literature with the hard-templating approach, is frequently used to create 3D macroporous replica, also called the inverse opal structures. CCT is based on the formation of a colloid crystal of close-packed and uniformly sized spheres (polymers or silica) with the interstitial spaces filled with the inorganic precursors or preformed nanoparticles (NPs).

Despite the remarkable properties of fluorinated materials and their well-established large application domains in heterogeneous catalysis,[11−14] energy production and storage,[15] microelectronics, and photonics,[16] these well-controlled synthetic strategies described above are sparsely applied for the elaboration of 3D porous fluorinated materials. Indeed, the soft-templating method was only reported for the synthesis of mesoporous MgF_2 thin films using polyvinyl acetate[17] or amphiphilic block copolymers as the structure-directing agent to introduce controlled mesoporosity.[18] The synthesis of $(Ca,Sr,Ba)F_2$,[8] $NaYF_4$:Eu, Tb,[10] and LaF_3[9] nanowires by the hard-templating method using different porous molds (SBA-15 and Al_2O_3) was reported in the 2000s. Finally, the most applied templating route for the synthesis of porous fluorides is the CCT method using poly(methyl methacrylate) (PMMA) or polystyrene (PS) spheres. Indeed, in the last decade, the preparations of macroporous doped-$NaYF_4$,[19−21] MgF_2, CaF_2, AlF_3,[22] and lanthanide oxyfluorides[23] were reported. Such sparse literature on organized porous inorganic fluorides (OPIFs) confirms unequivocally that these materials represent

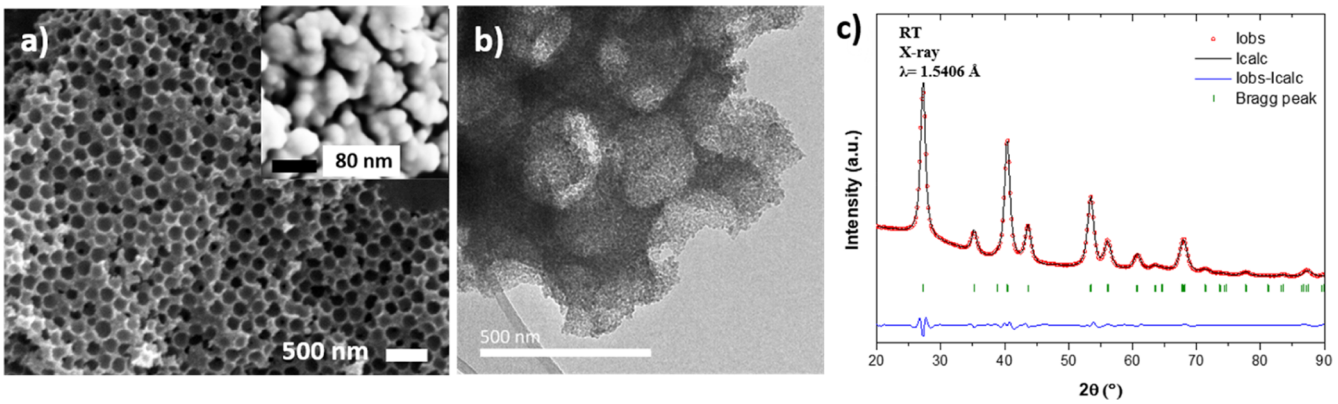

Figure 3. (a) SEM and (b) TEM images of macroporous MgF_2 OPIF-200. (c) Le Bail refinements of OPIF-200 after calcination under air at 375 °C and under F_2. Vertical markers give the Bragg peak positions of the tetragonal space group $P4_2/mnm$ (no. 136).

a new class of porous materials to be explored. This lack of study on the elaboration of 3D porous fluorides could be explained by the poor stability of fluorides at high temperature and the difficult preparation of fluoride NPs smaller than 10 nm,[14,24,25] which could be used as building blocks for porous material preparation.

In this paper, we report on the successful and unprecedented preparation of tunable pore-sized OPIFs as exemplified for MgF_2. For the first time, macroporous MgF_2 with a surface area of above 200 $m^2\ g^{-1}$ and mesoporous MgF_2 powder were prepared and carefully characterized. Almost not applied on fluorides, the synthetic route is based on the assembly of two building blocks: the polymer template and preformed MgF_2 NP, which is depicted in Figure 1. After subsequent calcinations of the OPIF composite material under air and F_2, carbon-free and slightly hydroxylated MgF_2 OPIFs are obtained. We present the pioneering application of these OPIF materials as heterogeneous catalysts for the gas-phase fluorination of the 2-chloropyridine under HF as the fluorinating agent. Indeed, MgF_2 NPs have attracted strong interest as catalysts for a variety of organic reactions[26−32] such as dehydrochlorination and dehydrofluorination reactions,[27] the acylation of 2-methylfuran by acetic anhydride,[29] or the fluorination of chlorinated reactants[11,12] and a catalyst support for gas-phase reaction such as dehydrofluorination reaction[33] or the fluorination of 1,1,1,3-tetrachloropropane with HF to 3,3,3-trifluoropropene,[13] for example.

2. RESULTS AND DISCUSSION

2.1. Synthesis and Characterization of MgF_2 OPIFs. As shown in Figure 1, our synthetic methodology to target OPIF MgF_2 porous materials comprises four steps: (i) syntheses of the two building blocks (fluoride NPs and polymer template) and their dispersion as a homogenous aqueous colloidal mixture, (ii) fluoride NP/polymer template assembly process via solvent evaporation to obtain the OPIF composite, (iii) calcination including concomitant polymer removal and inorganic fluorinated network densification, and (iv) final thermal treatment under F_2 to remove the carbon residue.

2.1.1. Step 1: Preparation of the Two Buildings Blocks (MgF_2 NPs and the Polymer Templates) and Their Colloidal Dispersion. In the first step, MgF_2 NPs were synthesized via a microwave-assisted solvothermal route using aqueous HF (40%) as the fluorinating agent, methanol as the solvent, and magnesium nitrate as the metal precursor at 90 °C for 30 min according to the reaction[11]

$$Mg(NO_3)_2 + 2HF \rightarrow MgF_2 + 2HNO_3$$

The profile refinement of the powder X-ray diffraction (PXRD) pattern confirms the rutile-type crystal structure of MgF_2 NPs (space group $P4_2/mnm$) with cell parameters a = 4.6544(6) Å and c = 3.0476(3) Å (JCPDS 01-072-1150, Figure 2). A diameter of about 7 nm was determined from PXRD refinement (D_{XRD}) and transmission electron microscopy (TEM) analysis (Figure 2, D_{TEM}). PMMA and PS were chosen as the template due to their facile thermal decomposition at temperature lower than 400 °C (Figure S1). To access to homogeneously sized polymer spheres with a tunable diameter, three different polymerization processes were used: surfactant-free emulsion polymerization and conventional emulsion polymerization to obtain macrosized polymer templates[25,34−36] and microemulsion polymerization for the polymer templates with a diameter of under 100 nm.[35] Home-synthetized polymer template latexes present the advantage of low polydispersity (PDI) in size and a controlled surface through the absence (surfactant-free emulsion polymerization) or the presence (conventional emulsion polymerization) of a surfactant (SDS, sodium dodecyl sulfate). Furthermore, the choice of the initiator in comparison with commercial latex (ammonium persulfate $(NH_4)_2S_2O_8$ vs potassium persulfate $K_2S_2O_8$) allows the decomposition without a K_2SO_4 residue. Electronic microscopy analyses show the obtention of spheres with diameters of ≈200 nm (PMMA), ≈85 nm (PMMA−SDS), and ≈45 nm (PS−SDS) (Figure S2). These aqueous latexes are stable as evidenced by a negligible change in polymer bead size after 1 month, as confirmed by dynamic light scattering (DLS, see Figure S3).

The dispersion of the NP and polymer template as a homogenous aqueous colloidal mixture aims to ensure uniform templating with evenly distributed pores through the OPIF material. The MgF_2 NP was dispersed in water, and the stability of the NP sol was investigated by DLS (Figure 2). Hydrodynamic diameters (D_h) of pristine NPs are about 200 nm. They increase and reach about 300 nm after 10 min, suggesting the formation of aggregates (Figure 2c). After 20 min, aggregate sedimentation occurs, and only smaller agglomerates (with the diameter ranging from 20 to 30 nm) remain in suspension. Upon the addition of trifluoroacetic acid (TFA) as the stabilizing agent, D_h values are significantly

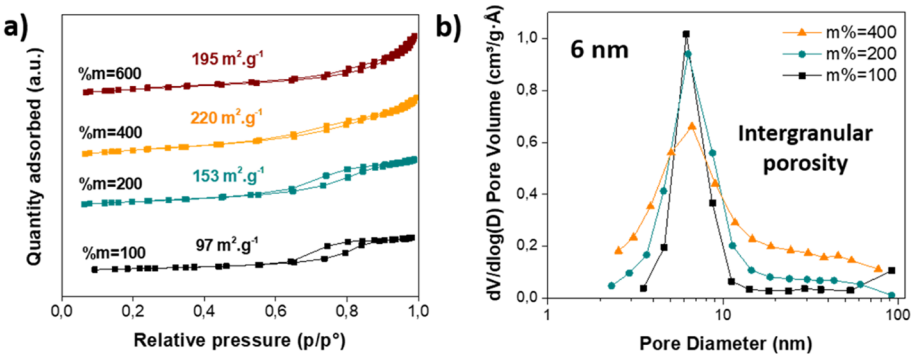

Figure 4. (a) N_2 adsorption−desorption isotherms of OPIF-200 with different % *m*. (b) Corresponding BJH pore size distributions.

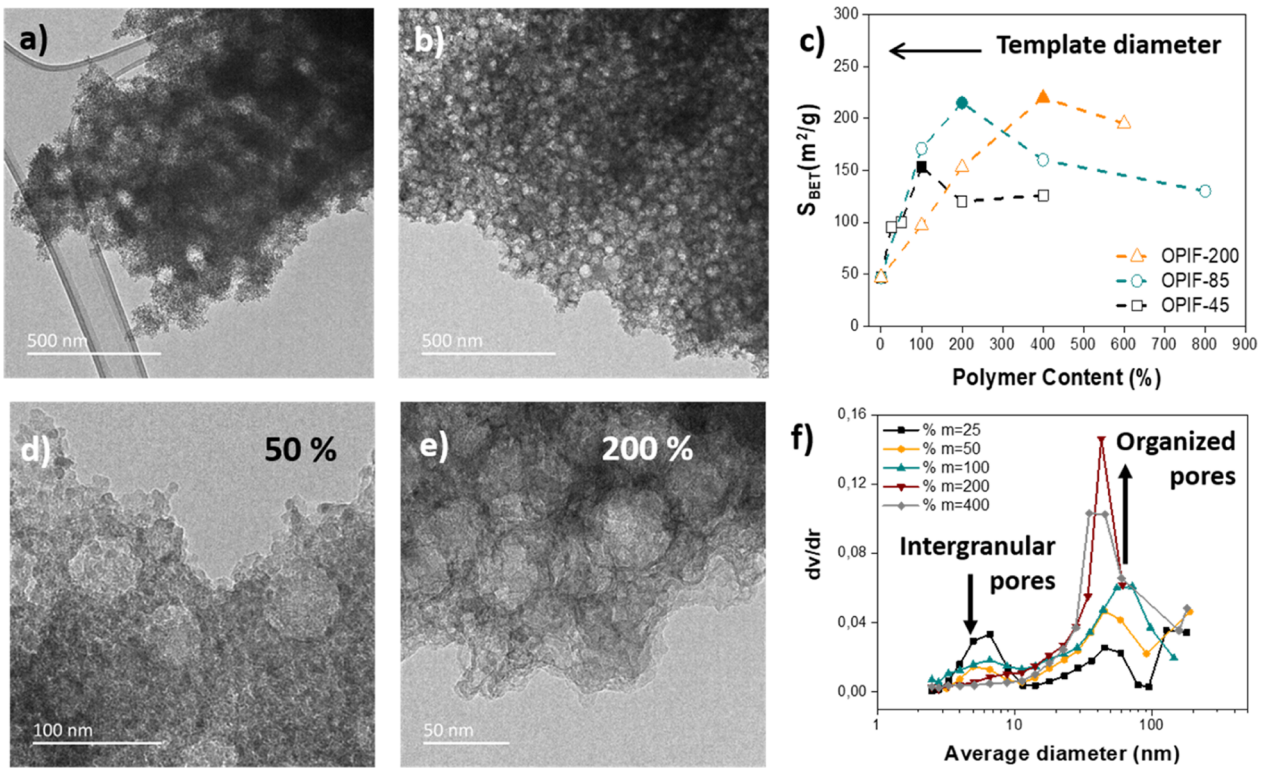

Figure 5. TEM images of (a) OPIF-85 and (b) OPIF-45 and (c) S_{BET} of MgF_2 OPIF materials synthesized using three polymer templates (OPIF-200 in orange, OPIF-85 in blue, and OPIF-45 in black) with varied polymer contents (% *m*). Solid points correspond to OPIF materials with the highest S_{BET}. TEM images of OPIF-45 with (d) % *m* = 50 with porosity coming from the organized pores and intergranular pores and (e) % *m* = 200 with porosity coming solely from organized pores. (f) BJH pore size distribution from the adsorption branch of the N_2 sorption isotherm.

reduced to 25 nm and remain unchanged for at least 30 min. This supports the ability of TFA to prevent NP agglomeration (Figure 2d). This phenomenon can be explained by the increase in positive zeta potential (ζ) of the MgF_2 NP (ζ = 40 mV)[37] with the pH decrease induced by TFA. Indeed, the NP stability in solution is ensured by higher repulsive particle interactions due to the enhanced surface charge, preventing from agglomeration.[38]

2.1.2. Preparation of MgF_2 OPIFs with Tunable Pore Sizes. The polymer template dispersed in water was added to this TFA-treated MgF_2 NP sol. Centrifugation and solvent evaporation were performed to assemble the NP with the polymer template and to obtain an OPIF composite, as depicted in Figure 1, step 2. The resulting composite material was calcined under air at 375 °C to remove the template and to obtain porous OPIF materials (step 3). The macroporous MgF_2 OPIF was successfully prepared [scanning electron microscopy (SEM) and TEM, Figure 3] using a PMMA template with a diameter of ≈200 nm (OPIF-200). The OPIF-200 is homogeneously templated with a pore diameter of around 200 nm corresponding to the PMMA diameter. TEM/SEM images evidenced the macroporosity and mesoporosity emerging from the voids between the NPs of the OPIF walls.

The PXRD diagram shows that the MgF_2 crystal structure is preserved after thermal treatment under air, and TEM analysis reveals that the walls are composed of MgF_2 NPs with D_{TEM} ≈ 9 nm, consistent with the crystallite size obtained from PXRD Le Bail refinements (D_{XRD} = 7 nm, Table S2). It is important to note that the structuration of the OPIF composite (NP + template) considerably slows down the crystallite growth during thermal treatment under air. Indeed, the calcination under air at 350 °C of pristine MgF_2 NPs leads to MgF_2 NPs (*NP-ref-OPIF* in the following) with a diameter of ≈18 nm, inducing a large decrease in the specific surface area from 320

Table 1. Specific Surface Areas (S_{BET}), NP Diameter (NP D), V_{total}, and V_{int} of OPIF Samples before and after F_2 Thermal Treatment

	before F_2				after F_2				after HF	
	S_{BET} ($m^2 g^{-1}$)	[a]NP D (nm)	[b]V_{total} (cm^3/g)	V_{inter} (cm^3/g)	S_{BET} ($m^2 g^{-1}$)	[a] NP D (nm)	[b]V_{total} (cm^3/g)	V_{inter} (cm^3/g)	S_{BET} ($m^2 g^{-1}$)	[a]NP D (nm)
NP-ref-OPIF	45(5)	16	0.19	0.06	45(5)	17	0.19	0.07	45(5)	20
OPIF-200	155(5)	10	0.37	0.29	140(5)	10	0.35	0.25	60(5)	15
OPIF-85	215(5)	9	0.76	0.41	130(5)	10	0.54	0.34	65(5)	15
OPIF-45	155(5)	9	0.46	0.12	75(5)	11	0.49	0.05	60(5)	15

[a]NP D determined by TEM/XRD. [b]Total cumulative pore volumes (V_{tot}) were calculated at $p/p^0 = 0.99$.

to 45 $m^2 g^{-1}$ (Figure S4). After nanostructuration of the NP into OPIFs, the specific surface area (S_{BET}) only decreases from 320 to 220 $m^2 g^{-1}$ for OPIF-200-200%, for example.

As the final porous morphology and S_{BET} depend on the template content, different polymer to particle mass ratios (m % = $m_{polymer}/m_{NP}$ = 100, 200, 400, and 600) were tested. Increasing m % improves the homogeneity of pore distribution (Figure S5). The S_{BET} reaches a maximum of 220 $m^2 g^{-1}$ for m % = 400 but slightly decreases to 195 $m^2 g^{-1}$ for m % = 600. To gain more insights into the porous structure, N_2 adsorption−desorption isotherms were recorded (Figure 4a). According to the IUPAC classification,[39] MgF_2 OPIFs have type IV isotherms for % m = 100, 200, and 400 with a hysteresis loop at relative pressure p/p^0 between 0.6 and 0.9 which correspond to the mesoporous material. This mesoporosity is associated with the intergranular pores between the MgF_2 NPs forming the walls, as confirmed by TEM and SEM analysis (Figure 3). The Barrett−Joyner−Halenda (BJH) model applied for type IV profiles on the desorption branch implies a monomodal pore size distribution centered at 6 nm (Figure 4b). The OPIF with % m = 600 shows a type II curve, characteristic of nonporous or macroporous materials. The absence of type IV is probably related to the loss of the intergranular porosity combined with the partial collapse of the structure due to the thinness of the walls leading to a decrease in the surface area. We conclude that the porosity in OPIF materials comes both from the 3D porous structure and the interspaces between NPs. In the rest of the manuscript, the porosity from the main pores and from the interspaces will be named organized porosity and intergranular porosity, respectively.

OPIF materials were also prepared using templates with smaller diameters. As already mentioned, two polymer templates were synthesized by conventional emulsion polymerization using SDS as the surfactant: PMMA with a diameter of 85 nm (PMMA−SDS) and PS with a diameter of 45 nm (PS−SDS). Various polymer to particle mass ratios (% m) led to highly organized porous MgF_2 OPIFs (respectively, named OPIF-85 and OPIF-45 in the following, Figure 5a,b). The S_{BET} evolution of OPIF-85 and OPIF-45 with the % m is shown in Figure 5c and compared with that of OPIF-200. The decrease in the template size shifts the optimum polymer content (blue circle) to 200% (S_{BET} = 215 $m^2 g^{-1}$) for OPIF-85 and to 100% for OPIF-45 (S_{BET} = 155 $m^2 g^{-1}$).

Both OPIF-85 and OPIF-45 show type IV nitrogen sorption isotherms for different % m (Figure S6). The pore size and its evolution as a function of polymer content were carefully studied by the BJH method. In the case of OPIF-85, only the intergranular porosity could be observed ($d \approx 6-11$ nm) as the diameter of organized pores is out of range (>50 nm) for this analysis (Figure S7). For OPIF-45, the organized porosity (pore diameter ≈ 45 nm) is confirmed, as shown in Figure 7a. It is interesting to note that by increasing % m, a transition from bimodal (organized pores + intergranular pores) to monomodal (organized pores) pore distribution is observed. This difference of the porous structure is confirmed by TEM. Indeed, the presence of the intergranular mesoporosity is observed between the NPs with low polymer content (50%, Figure 5d), while individual NPs are no longer observable in 200% (Figure 5e). This observation coupled with the abrupt reduction of S_{BET} beyond 100% in OPIF-45 suggests that the structural change is not only linked to the variation of polymer content but also depends on the presence of intergranular porosity.

The intergranular volumes (V_{int}) were calculated by subtracting cumulative pore volumes of pores with a width of >10 nm (V_{or}) from the total cumulative pore volumes ($V_{int} = V_{total} - V_{or}$). Figure S8 shows V_{int} and V_{or} as a function of % m, demonstrating a maximum−minimum relation with the polymer content. Indeed, the obtention of high S_{BET} is a compromise between organized and intergranular pores where the highest S_{BET} for each template size occurs when $V_{int} + V_{or}$ (*i.e.*, V_{total}) is maximized. To validate the beneficial effect of intergranular pores on the S_{BET}, OPIF-45 with m = 100% was prepared by the removal of the polymer template with tetrahydrofuran (THF) (Figure S9). When the PS is removed chemically, the volume of the intergranular porosity ($V_{int\text{-}thermal}$ = 0.12 $cm^3 g^{-1}$; $V_{int\text{-}THF}$ = 0.25 $cm^3 g^{-1}$) and the S_{BET} increased ($S_{BET\text{-}thermal}$ = 155 to $S_{BET\text{-}thermal}$ = 180 $m^2 g^{-1}$). These results evidence the densification of the NP network during removal of the template by thermal treatment, therefore confirming that the S_{BET} strongly relies on both intergranular porosity and organized porosity.

2.1.3. Calcination under F_2 for Carbon Residue Removal. OPIF samples with different pore sizes and with the highest surface areas were selected for a subsequent thermal treatment under F_2 gas to remove the carbon residue ($C + 2F_2 \rightarrow CF_4$) and eventual hydroxyl groups ($2OH^- + F_2 \rightarrow O_2 + 2HF$). Indeed, the residual carbon could affect the porous structure and the S_{BET} and block the active sites for the transformation of 2-chloropyridine. The selected OPIFs were OPIF-85: 200% and OPIF-45: 100%. For OPIF-200, 200% was selected as it allows the preparation of MgF_2 OPIFs with high S_{BET} and lower carbon content (Figure S10). After thermal treatment under F_2, the color changed from brown to white and this carbon removal was confirmed by Fourier transform infrared (FTIR) spectroscopy analysis (Figures S11 and S12). Before F_2 treatment, all FTIR spectra exhibit bands at 1405 cm^{-1} assigned to stretching vibrations of the CO_3^{2-} groups.[23] The bands at 1150 cm^{-1} are associated with the C−F groups.[23] Two bands are also observed at 3393 and 1598 cm^{-1} corresponding to −OH of hydroxyl groups or adsorbed

water molecules on the OPIF surface. After F_2 thermal treatments, the removal of the CO_3^{2-}, C−F, and −OH groups is evidenced by the disappearance of the related bands. TEM investigations showed the stability of the porous structure under F_2 despite a decrease in the specific surface area (Figure S13 and Table 1). The S_{BET} of the macroporous OPIF (OPIF-200 and OPIF-85) remains above 130 $m^2\ g^{-1}$ (D_{XRD} = 10 nm) even after the harsh thermal treatment under F_2. In comparison, NP-ref-OPIF shows the largest particle size (16 nm) and a three times smaller specific surface area after F_2 treatment, emphasizing the importance of 3D structuration on the thermal stability by introducing organized and intergranular pores. This stability could be explained by the presence of pores which could prevent particle mobility and therefore NP sintering.

2.2. Modification of the Physicochemical Properties of OPIF Samples after HF Treatment. *2.2.1. Characterization by PXRD, N_2 Sorption, TEM, and ^{19}F and ^{1}H Solid-State MAS NMR.* Prior to catalytic transformation of 2-chloropyridine under a HF atmosphere, the catalysts were activated *in situ* by HF for 1 h at 350 °C (activation step). This step corresponds to the stabilization of the materials under a HF atmosphere and allows us to characterize the properties (amount and strength) of the active sites involved in the Cl/F exchanges. The influence of this treatment on the structural properties of OPIF samples was first investigated by PXRD, N_2 sorption, and TEM. Despite the severe condition, the rutile phase of MgF_2 is preserved under HF (Figure S14). Unfortunately, this step induces an adverse effect as the S_{BET} decrease to ≈60 $m^2\ g^{-1}$ related to a particle size increase to 15 nm (Table 1, TEM in Figure S15) which is close to NP-ref-OPIF (S_{BET} of 45 $m^2\ g^{-1}$ and particle size of 20 nm).

Further structural information was obtained from ^{19}F and ^{1}H solid-state MAS NMR studies of samples OPIF-45 before and after the HF activation step, OPIF-85, OPIF-200, and NP-ref-OPIF after HF treatment. The nuclear magnetic resonance (NMR) spectra are reported in Figure 6 and compared with the pristine MgF_2 NP (without the calcination step) that we recently studied,[11] that is, MgF_2 NP prepared from the nitrate precursor, after HF activation. For the rutile-type crystal structure of MgF_2 involving a single F crystallographic site,[40] a single ^{19}F NMR line is expected and observed [at δ_{iso} (isotropic chemical shift) = −197.3 ppm] on its spectrum.[41] In contrast, all ^{19}F spectra presented in Figure 6 exhibit one main asymmetrical line with a maximum at a similar value (δ_{iso} ≈ −197.7 ppm) and a shoulder toward higher δ_{iso} values (three resonances with close δ_{iso} values are necessary to reconstruct the spectra correctly). In addition, a second contribution appears distinctly at about −183 ppm and even (except for MgF_2 NPs prepared from the nitrate precursor, after HF activation) a third contribution appears at about −178 ppm (Figure 6, fits and results of these fits are given in Figure S16 and Table S3). Moreover, compared with the ^{19}F NMR line of a microcrystalline sample (line width of 795 Hz),[11] these lines are broader (line widths from 853 Hz for MgF_2 NPs prepared from the nitrate precursor, after HF activation, to 1032 Hz for OPIF-45 before HF activation) (Figure S17). This broadening mirrors chemical shift distributions due to disorder around fluorine atoms in relation with the slightly higher specific surface area (from 45 to 75 $m^2\ g^{-1}$) and partial hydroxylation, the latter resulting additionally in the shoulders and contributions at high ^{19}F δ_{iso} values. The increase in the ^{19}F δ_{iso} value with the hydroxide content, that is, the number of

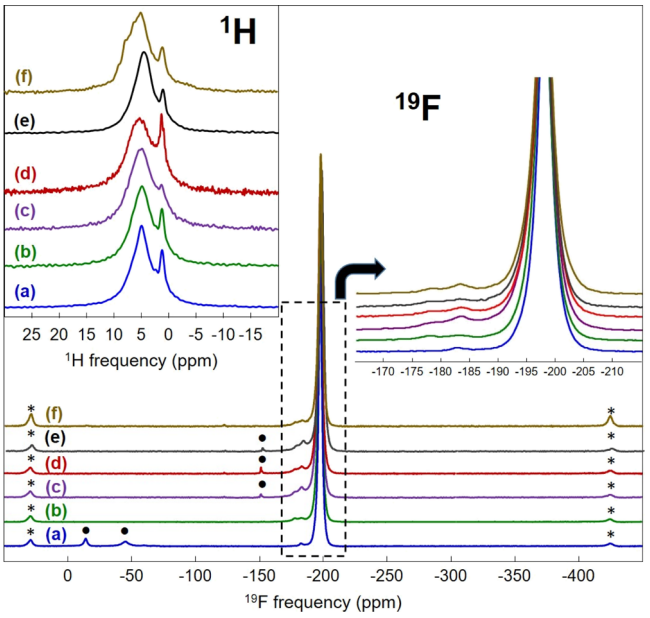

Figure 6. ^{1}H solid-state MAS NMR spectra (inset) and ^{19}F solid-state MAS (64 kHz) NMR spectra of (a) MgF_2 NPs prepared from the nitrate precursor, after HF activation, (b) NP-ref-OPIF, OPIF-45 before (c) and after (d) HF activation, OPIF-85 (e), and OPIF-200 (f), after HF activation. The isotropic lines of the ^{19}F spectra are expanded in the inset on the right. The star symbols indicate the spinning sidebands. The dot symbols (a−e) indicate fluoride impurities of (a) MgF_2 NPs prepared from the nitrate precursor, after HF activation (60 kHz), (b) NP-ref-OPIF, OPIF-45 (64 kHz), (c) before (60 kHz) and (d) after (64 kHz) HF activation, OPIF-85 (e), and OPIF-200 (f), after HF activation.

hydroxyl groups in the environment of the fluoride ion in hydroxyfluorides, is a well-known phenomenon which has been observed in magnesium hydroxyfluorides (up to 40 ppm).[42] Nevertheless, due to the very large number of different environments of fluoride ions in partially hydroxylated magnesium fluorides, $MgF_{2-x}(OH)_x$, the assignment of the additional lines seems to be unrealistic. Indeed, due to the presence of eleven anions as the next nearest neighbors at four different distances (ranging from 2.58 to 3.35 Å, Table S4[40]), there are several inequivalent $FMg_3F_{11-y}(OH)_y^{6-}$ environments for each of the ten $0 < y < 11$ values. In any case, the proportion of fluoride ions in the fluoride (FMg_3F_{11}) environment can be estimated within the range 86−68 with, in decreasing order, the samples after HF activation: MgF_2 NPs prepared from the nitrate precursor (86%), NP-ref-OPIF (78%), OPIF-200 (74%), OPIF-45 (71%), and OPIF-85 (68%) and then OPIF-45 before HF activation (Table S3 and Figure S16). Assuming a random distribution of OH^- and F^- ions at anionic sites (Table S5), only rates of OH groups ranging from ≈1.5 to 3.5% ($0.03 \le x \le 0.07$) satisfy such proportions of the FMg_3F_{11} environment. Even if they are slightly superior to that of NP-ref-OPIF and to that of MgF_2 NPs prepared by microwave-assisted solvothermal synthesis and activated under HF[11] (including MgF_2 NPs prepared from the nitrate precursor), the rates of OH groups in the OPIF samples, before and after HF activation, remain low.

The ^{1}H solid-state MAS NMR spectra of all MgF_2 samples (Figure 6, fits and results of these fits in Figure S18 and Table S6) present one main broad contribution (ranging from 0 to 10 ppm) with δ_{iso} values at the maximum ranging from 4.5 to 5

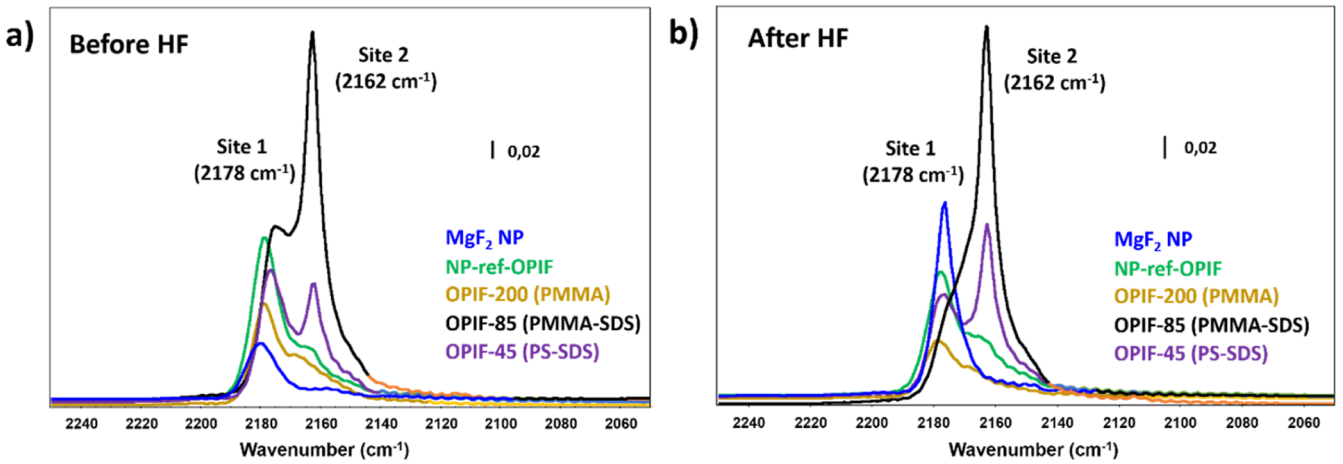

Figure 7. CO adsorption followed by IR over OPIF catalysts (a) before and (b) after HF treatment.

ppm, assigned to surface-adsorbed H_2O molecules and/or OH groups where hydrogen atoms are involved in H-bonds and a smaller contribution with δ_{iso} values at the maximum ranging from 1.1 to 1.2 ppm, assigned to Mg_3−OH environments where hydrogen atoms are not involved in H-bonds.[43] However, the main contribution of the spectra of the OPIF-45 samples before and after HF activation is broader, whereas those of OPIF-85 and OPIF-200 after HF activation are narrower. Moreover, the latter two have an additional contribution at higher δ_{iso} values (≈6 or ≈8 ppm). These differences which reflect different chemical shift distributions are difficult to interpret since these samples have similar specific surfaces. At last, the spectra of the OPIF-45 samples differ from each other by the larger relative intensity of the contribution assigned to Mg_3−OH environments after activation (13.4 vs 10.0%; Table S6) but above all by a smaller intensity of the NMR spectrum (evidenced by the lower signal-to-noise ratios although recorded with the same number of transients). This can be explained by a decrease in the amount of adsorbed H_2O molecules, related to the decrease in the specific surface area of the NPs (75 vs 60 m^2 g^{-1}; Table 1).

2.2.2. Characterization of the Actives Sites by CO Adsorption Followed by IR. The properties (quantity and strength of Lewis acid sites) of the catalytic sites were characterized by adsorption of CO as the probe molecule followed by IR spectroscopy before and after the activation step by HF (Figure 7). CO is a suitable probe molecule for the characterization of Lewis acidity as the (CO) vibration frequency is very sensitive to the local cationic environment of the coordinatively unsaturated magnesium centers.

All samples show the presence of coordinatively unsaturated magnesium centers where CO can be adsorbed. For the MgF_2 NP prepared from the nitrate precursor,[11] NP-ref-OPIF, and OPIF-200, a CO adsorption band was mainly observed at 2178 cm^{-1} (site 1). Interestingly, OPIF-85 and OPIF-45 clearly present two CO adsorption bands centered at 2178 cm^{-1} (site 1) and 2162 cm^{-1} (site 2) with different intensities before and after HF activation. These bands are attributed to two different magnesium environments corresponding to two types of low (site 2) to intermediate (site 1) strength of CO adsorption sites. According to Wuttke et al.,[44] the presence of these bands at 2178 and 2162 cm^{-1} corresponds to tetracoordinated (Mg_{4c}^{2+}) and pentacoordinated (Mg_{5c}^{2+}) magnesium atoms located in the edge and in-plane of a crystal of MgF_2, respectively. After HF treatment (Figure 7b), the intensity of the higher strength Lewis acid site (site 1) decreased in favor of the weaker sites (site 2) (Table 2). This evolution

Table 2. FTIR CO Characterization of Various MgF_2 Samples[a]

	before HF			after HF		
	Q_{sites_T}	Q_{sites_1}	Q_{sites_2}	Q_{sites_T}	Q_{sites_1}	Q_{sites_2}
MgF_2 NPs prepared from the nitrate precursor[11]	79	79	0	90	90	0
NPs-ref-OPIF	201	114	87	123	52	71
OPIF-200	203	81	122	117	117	N.A.
OPIF-85	525	183	342	328	76	252
OPIF-45	318	133	185	226	81	145

[a]Quantification of sites (μmol g^{-1}), Q_{sites_T}: total quantity of sites; Q_{sites_1}: quantity at 2178 cm^{-1}; and Q_{sites_2} at 2162 cm^{-1} (N.A., nonapplicable). Estimated relative uncertainty: 10%.

corresponds to a change in the coordination degree of magnesium atoms from 4 to 5 and to a favored adsorption of CO on sites located in-plane of a crystal of MgF_2. The presence of site 2 in a larger amount could be explained by the higher amount of SDS surfactant used during the conventional emulsion polymerization synthesis for the synthesis of PMMA−SDS (85 nm) and PS−SDS (45 nm). Indeed, localized Na and S were evidenced by energy-dispersive X-ray (EDX)−TEM analysis (Figure S18). Regarding the quantification of these sites by the integration of the corresponding bands, an increase in the total number of active sites from 79 to 201 μmol g^{-1} is observed between MgF_2 NPs prepared from the nitrate precursor and NPs-ref-OPIF; this might be influenced by the addition of TFA for the preparation of NPs-ref-OPIF. This statement will be further investigated. Regarding the OPIF materials, a significant gain in the number of total sites to 525 μmol g^{-1} is achieved for OPIF-85 corresponding to the OPIF with the highest total cumulative pore volumes (V_{tot}) (Table 1). After HF activation, a decrease in the total number of sites is observed for all samples. The amount of site 2 remains higher than that of site 1 except for OPIF-200 (PMMA). The same tendency is observed for the number of sites per surface area (Table 3).

Table 3. Concentration Sites μmol m^{-2} ($C_{sites\_T} = C_{sites\_1} + C_{sites\_2}$; Site 1 at 2178 cm^{-1} and Site 2 at 2162 cm^{-1}) before and after Activation by HF (N.A., nonapplicable)

	before HF			after HF		
	C_{sites_T}	C_{sites_1}	C_{sites_2}	C_{sites_T}	C_{sites_1}	C_{sites_2}
MgF_2 NPs prepared from the nitrate precursor[11]	0.5	0.5	0	2.8	2.8	0
NPs-ref-OPIF	6.7	3.8	2.9	2.4	1.0	1.4
OPIF-200	1.5	0.6	0.9	1.9	1.9	N.A.
OPIF-85	5.2	1.8	3.4	5.2	1.2	4.0
OPIF-45	5.7	2.4	3.3	4.0	1.4	2.6

2.3. Catalytic Performances for the Transformation of 2-Chloropyridine.

MgF_2 OPIFs were tested for the first time as catalysts for the transformation of 2-chloropyridine measured at 350 °C in the presence of HF gas. All OPIF materials present a good ability with a 100% selectivity toward 2-fluoropyridine (2FPy) (Table 4). Unfortunately, the catalytic activity of OPIF materials and their reference (MgF_2-ref-OPIF) is similar (≈25 mmol h^{-1} g^{-1}), and this value is slightly lower than the catalytic activity obtained with MgF_2 from the nitrate precursor[11] (31 mmol h^{-1} g^{-1}). This result could be explained by the different amounts and strengths of the catalytic sites, given that all materials have the same specific surface area (≈60 m^2 g^{-1}). Indeed, for this reaction, the catalytic sites require a medium Lewis acid strength (CO adsorption band at 2176 cm^{-1}, site 1), confirming that MgF_2 NPs prepared from the nitrate precursor with a higher amount of site 1 corresponds to the highest activity per site (turnover frequency, TOF).[12] Therefore, even if site 2 may have a contribution to the catalytic activity, it seems to be lower. Further experiments are required to explain the origin of site 2 having a weak Lewis acidity together with the influence of Na and S traces on the catalytic properties. Despite the lower performance of MgF_2 OPIFs, a graduation of Lewis acidity strength could be valuable for other reactions as the catalytic activity depends on both the number and properties of active sites.

Table 4. Activity per Gram and per Surface Area for the Transformation of 2-Chloropyridine (T = 350 °C, t = 4h30, and HF/N_2/2-ClPy Molar Ratio = 6.4/1.7/1.0) and Estimated Relative Uncertainty: 5%

	activity		TOF
	mmol h^{-1} g^{-1}	mmol h^{-1} m^{-2}	h^{-1}
MgF_2 NPs prepared from the nitrate precursor[11]	31	0.63	340
NP-ref-OPIF	24	0.47	195
OPIF-200	27	0.43	230
OPIF-85	25	0.40	76
OPIF-45	25	0.40	102

3. CONCLUSIONS

MgF_2 OPIFs (S_{BET} > 150 m^2 g^{-1}) with tunable pore sizes (200, 85, and 45 nm) were synthesized, and highly organized mesoporous MgF_2 powder was obtained for the first time. The synthetic route is based on the assembly of two building blocks, homemade polymer templates and preformed MgF_2 NPs. After subsequent calcinations of the OPIF composite material under air and F_2, carbon-free MgF_2 OPIFs with a significant specific surface area were prepared. These OPIF materials were characterized at each synthesis step by PXRD, N_2 sorption, SEM and TEM analyses, and ^{19}F and ^{1}H solid-state NMR. This work shows that OPIF structures strongly rely on both the intergranular pore volume and template size. The MgF_2 OPIF with an organized pore size of 85 nm and an intergranular pore size of 9 nm exhibits the highest specific surface area (215 m^2 g^{-1}). Interestingly, the nanostructuration into OPIFs leads to a better stability of the surface area during thermal treatment under air or F_2 in comparison with MgF_2 NPs. As the first application, MgF_2 OPIFs were tested for the catalytic transformation of 2-chloropyridine under severe conditions (HF gas atmosphere, 350 °C). The OPIF activity, slightly lower than that of MgF_2 NPs, was related to the lower Lewis acidity strength of the part of active sites. The presence of these two kinds of sites represents a real originality which could be explored for other catalytic reactions requiring various active sites. In future work, as we successfully demonstrated that the nature and the size of the template could be tuned to prepare MgF_2 OPIF materials with different pore sizes, it will give access to the preparation of OPIF materials with pore diameters under 40 nm to exert a strong influence on the catalytic behaviors.

4. EXPERIMENTAL SECTION

4.1. Synthesis of the Polymer Templates. *4.1.1. Materials.* All reagents were purchased from Sigma-Aldrich and used as received unless otherwise noted. Methyl methacrylate (MMA, ≥99%), ammonium persulfate (APS, 98%), styrene (S, ≥ 99%), aluminum oxide (activated, neutral, Brockmann I), SDS (99%, Acros Organics), acetone (≥99.8%, VWR), and 1-pentanol (≥99%, Alfa Aesar) were used. MMA and S were passed through a column of aluminum oxide prior to polymerization. Ultrapure water was obtained from a PureLab ELGA system and had a resistivity of 18.2 MΩ cm^{-1} at 25 °C.

4.1.2. Polymer Template Syntheses and Characterizations. The free-emulsion polymerization of MMA was typically started by charging 0.2 g of APS as the initiator, 20 mL of acetone, and 60 mL of ultrapure water into a three-neck flask (reaction medium) that was connected to a reflux condenser and an ice bath. While the mixture was homogenized using a magnetic stirrer, nitrogen gas was purged to the reaction medium to remove free oxygen. After 30 min, 1 mL of MMA was added to the mixture, the temperature was increased to 70 °C, and the reaction continued for 4 h under nitrogen flow. Finally, the reaction medium was cooled down to room temperature, and the white polymer latex was used without purification. The D_h and PDI values of the resulting polymer template were measured by DLS: $(D_h)_{DLS}$ = 206 nm and PDI = 0.02. The PMMA beads were further characterized by SEM. A SEM image is shown in Figure S3a. This polymer template is named PMMA-200 nm.

For the conventional emulsion polymerization of MMA, 1.65 g of SDS was initially added to the reaction medium, and the previous method was followed. The polymer template dispersed in water was used without further purification. $(D_h)_{DLS}$ = 85 nm and PDI = 0.09. A SEM image of PMMA beads is shown in Figure S3b. This PMMA template is named PMMA-85 nm.

Microemulsion polymerization of styrene (S) was started by charging 33 mg of APS, 1.65 g of SDS, 1 mL of 1-pentanol, and 42 mL of ultrapure water in a three-neck flask connected to a reflux condenser and an ice bath. After 30 min of mixing under nitrogen flow, 7 mL of styrene was added to the mixture and temperature was increased to 70 °C. While nitrogen gas was purged to the flask, the reaction continued for 3 h. Synthesis was terminated by cooling down the flask to room temperature, and the polymer template was used without purification. $(D_h)_{DLS}$ = 44 nm and PDI = 0.05. A SEM image of PS beads is shown in Figure S3c. This PS template is named PS-45 nm.

4.2. Synthesis of MgF_2 NPs. Magnesium nitrate hexahydrate ($Mg(NO_3)\cdot 6H_2O$, 98%) and TFA (CF_3CO_2H) were purchased from Alfa Aesar. Hydrofluoric acid (HF, 40%) and methanol (CH_3OH, 99.8%) were purchased from Sigma-Aldrich. All reagents were of analytical grade and used as received without further purification. In a typical synthesis, 2.56 g of magnesium nitrate hexahydrate was dissolved in 2 mL of methanol in a Teflon reactor under stirring. Afterward, 0.88 mL of HF and 8 mL of methanol were added to the mixture and microwave heating was applied at 90 °C for 30 min. The resulting gel was washed with ethanol to remove any unreacted reagents and methanol and subsequently used for preparation of OPIF materials.

4.3. Synthesis of OPIF Materials. In general, 0.75 g of MgF_2 NP gel was sonicated in 20 mL of water to obtain a clear sol and 300 μL of TFA was added dropwise to the dispersion (2.75 mg mL^{-1} MgF_2 NP and maximum concentration tested, 5mg mL^{-1}). While stirring, a given amount of polymer template latex (PMMA-200 nm, PMMA-85 nm, and PS-45 nm as described in the previous section) was gradually added to the medium (Table S1). After stirring for 24 h, the resulting mixture was centrifuged at 800 rpm for 1 h, dried at 110 °C, and calcined at 375 °C for 2 h (heating rate 2 °C min^{-1}) under an air atmosphere to remove the template and densify the MgF_2 network. As a reference, MgF_2 NPs (NP-ref-OPIF) were prepared according to the technique described above without the addition of polymer latex, and they were used for catalyst tests.

Soxhlet extraction was utilized to chemically remove the polymer template (PS−SDS). A porous thimble loaded with the dried sample was placed inside the main chamber of the Soxhlet extractor. The extraction cycle was repeated for 24 h by refluxing the 70% (v/v) solution of THF through the thimble using a condenser with cold water entering at the bottom and exiting above. The extraction was terminated by cooling down the flask to room temperature. The sample was washed with distilled water and dried at 60 °C.

4.4. F_2 Treatment. The calcination of OPIF compounds under F_2 gas to remove the carbon residue was carried out in a specific equipment dedicated to molecular fluorine, automatically controlled in order to guarantee constant experimental conditions. The OPIF compound was spread evenly in a passivated nickel boat that was introduced in a nickel reactor surrounded by a classic horizontal split furnace. The samples were then dehydrated at 140 °C under dynamic primary vacuum followed by filling of the reactor with nitrogen. The temperature was set to T = 100 °C for OPIF-200 and T = 400 °C for OPIF-85 and OPIF-45, and a mixture of 10% F_2 in nitrogen (Air Liquide) was flowed through the reactor under dynamic conditions for 2 h before being flushed by nitrogen.

4.5. HF Activation and Catalytic Measurements. As described previously,[12,45] the activation by HF and the catalytic activity of the various MgF_2 materials for the transformation of 2-chloropyridine were carried out in a fixed-bed reactor. The different MgF_2 samples were diluted with 6 cm^3 of Lonza graphite (size grains between 125 and 200 μm). The catalyst was activated *in situ* by HF under nitrogen (HF/N_2 molar ratio: 1/4) for 1 h at 350 °C (activation step). Then, 2-chloropyridine was introduced into the reactor using a syringe pump. The partial pressures of the various components were 0.806 bar for HF, 0.075 bar for 2-chloropyridine, and 0.132 bar for nitrogen ($HF/2ClPy/N_2$: 10.8/1/1.7). The organic gas products were trapped into 1,2-dichloroethane. HF and HCl were quenched in an aqueous solution of potassium hydroxide at the outlet of the reactor. The organic components were analyzed with a Scion 456 gas-phase chromatograph (Bruker) equipped with a DB5 capillary column (inside diameter: 0.2 mm, thickness of the film: 1 μm, and length: 30 m). The oven temperature was increased from 100 to 200 °C at a rate of 5 °C min^{-1}.

The catalyst performances were compared at isoconversion of 2-chloropyridine lower than 25% in order to be in a differential regime. In all cases, only 2FPy was observed as the reaction product and HCl as the byproduct. Thus, the selectivity toward 2FPy was equal to 100% and the conversion of 2-chloropyridine corresponded to the 2FPy yield. In these experiments, the molar balance was always higher than 90%. No thermal decomposition of 2-chloropyridine was observed.

The catalytic activity A (mmol h^{-1} g^{-1}) was defined as the conversion of 2-chloropyridine multiplied by the flow of 2-chloropyridine (mol h^{-1}) and divided by the mass of the catalyst. The intrinsic catalytic activity Ai (mmol h^{-1} m^{-2}) was calculated by taking into account the specific surface area of the catalyst after the activation step by HF. The TOF (h^{-1}) was calculated from the catalytic activity (A: mmol h^{-1} g^{-1}) divided by the number of actives sites defined as coordinatively unsaturated metallic sites (Q_s: μmol g^{-1}) measured by CO adsorption followed by IR. Gaseous HF (cylinder of 800 g) was provided by Air Liquide, and 2-chloropyridine was provided by Sigma-Aldrich.

4.6. Technical Characterizations. *4.6.1. Dynamic Light Scattering.* The measure of D_h of polymer templates and MgF_2 NPs was conducted on a Nanosizer ZS Malvern device with a wavelength of 633 nm (Ne−He laser) at an angle of 173°. Each measure was repeated five times at 25 ± 1 °C with a delay of 60 s between the tests.

4.6.2. X-ray Diffraction. PXRD patterns of the MgF_2 NPs were recorded with a PANalytical θ/θ Bragg−Brentano Empyrean diffractometer (Cu $K\alpha_{1+2}$ radiations) equipped with a PIXcel1D detector. Data were collected in the [15−110°] 2θ angle range for a total acquisition time of 3 h with 0.499° steps. The NIST Standard Reference Material LaB_6 (NIST SRM 660b) was used to take into account the instrumental broadening. The PXRD pattern of LaB_6 was recorded with the conditions (step and counting time) used for the analysis of MgF_2 samples. PXRD patterns were fitted using the Le Bail method[46] implemented in the Fullprof program.[47] The line broadening due to the nanometric size of the sample was calculated using the Thompson−Cox−Hastings pseudo-Voigt function[48] that includes size and strain-broadening terms for both Lorentzian and Gaussian components. The two parameters (Y and F) of the Lorentzian component of this function were refined to calculate the apparent crystallite size $\langle L \rangle$ calculated by Fullprof using Langford's method.[49] The diameter D_{XRD} of the spherical particles is related to $\langle L \rangle$ using the following formula $D_{XRD} = 4/3 \times \langle L \rangle$.

4.6.3. Scanning Electron Microscopy. SEM images were obtained either using a JEOL microscope (JSM 6510 LV) at 20 kV or a Zeiss SUPRA 55-VP microscope at an acceleration voltage of 5 kV. All samples were coated by gold or gold/palladium (70/30) before analysis. The mean pore diameters were deduced by statistical evaluation of about 100 particles using ImageJ software.[50]

4.6.4. Transmission Electron Microscopy. TEM studies were performed on a JEOL JEM 2100 HR electron microscope operating at 200 kV. The samples for transmission electron microscopy investigation were prepared by ultrasonically dispersing the raw powders in ethanol, depositing a drop of the resulting suspension onto a holey carbon-coated copper grid, and finally drying the grid in air. Mean diameters of the NPs (D_{TEM}) or pores were deduced by statistical evaluation of about 100 particles using ImageJ software.[51]

4.6.5. ^1H and ^{19}F and Solid-State MAS NMR. ^1H and ^{19}F solid-state MAS NMR experiments were performed on a Bruker Avance III spectrometer operating at 7.0 T (^1H and ^{19}F Larmor frequencies of 300.1 and 282.4 MHz, respectively), using a 1.3 mm CP-MAS probe head. The ^1H and ^{19}F MAS spectra were recorded using a Hahn echo sequence with an interpulse delay equal to one rotor period. The 90° pulse lengths were set to 2.4 and 1.25 μs; the recycle delays were set to 120 and 900 s; and 24 to 64 and 32 to 48 transients were accumulated for ^1H and ^{19}F, respectively. ^1H and ^{19}F spectra refer to TMS and $CFCl_3$, respectively, and they were fitted using DMFit software.[52]

4.6.6. N_2 Sorption. The OPIF specific surface areas were measured at 77 K using a TriStar II 3020 (Micromeritics). The powders were degassed under vacuum at 100 °C for 12 h prior to measurement. The S_{BET} was calculated using the Brunauer−Emmett−Teller (BET) method. The porosity was evaluated from desorption branches of the N_2 isotherms using the BJH model. The total pore volumes were estimated from the adsorbed amount at the relative pressure p/p^0 = 0.99.

4.6.7. FTIR Spectroscopy. FTIR spectra of OPIFs after F_2 treatment were collected in air at room temperature with a Bruker Alpha FT-IR spectrometer equipped with the Platinum QuickSnap ATR sampling module. The spectral resolution is 4 cm^{-1} in the 400−4000 cm^{-1} range.

As described previously,[11] CO adsorption was followed by FTIR on a ThermoNicolet NEXUS 5700 spectrometer with a resolution of 2 cm^{-1}, and 64 scans per spectrum were collected. Samples were pressed into thin pellets (10−60 mg) with a diameter of 16 mm and pretreated *in situ* during one night under nitrogen at 300 °C. After that, the cell was cooled down with liquid nitrogen to 100 K. A background spectrum was collected which was then subtracted from the following spectra obtained after CO adsorption. Then, successive doses of CO were introduced quantitatively, and an infrared spectrum was recorded after each adsorption until saturation. The final spectrum was recorded with 1 Torr of CO at equilibrium pressure (saturation). All spectra were normalized to an equivalent sample mass (25 mg). The quantification of the amount of Lewis acid sites Q_s (μmol g^{-1}) was carried out by the integration of the total area of the IR bands at saturation between 2100 and 2200 cm^{-1} using the molar absorption coefficient ε determined for MgF_2 and equal to 1.53 μmol cm^{-1}.[45]

■ ASSOCIATED CONTENT

Supporting Information

The Supporting Information is available free of charge at https://pubs.acs.org/doi/10.1021/acsanm.1c01768.

XRD patterns and results of Le Bail refinements of MgF_2 NPs and OPIF materials, analysis of polymer templates (PMMA and PS) by TGA, MEB/TEM and DLS, DLS of MgF_2 NPs dispersed in water, MEB of OPIF-200 with different *m* % ratios, N_2 adsorption−desorption isotherms and BJH of OPIF-85 and OPIF-45 with different template contents, TEM and N_2 analysis of OPIFs obtained by chemical removal of the polymer template, pictures and FTIR of the OPIF catalyst before and after F_2 thermal treatment, TEM images of OPIF-200 after F_2 and HF treatment, ^{19}F and ^{1}H MAS NMR spectra of the different OPIF materials, and TEM−EDX of OPIF-45 (PS-SDS) after HF activation (PDF)

■ AUTHOR INFORMATION

Corresponding Authors

Sylvette Brunet − *Institut de Chimie des Milieux et Matériaux de Poitiers (IC2MP), UMR 7285 CNRS, Université de Poitiers, 86073 Poitiers Cedex 9, France*; Email: sylvette.brunet@univ-poitiers.fr

Amandine Guiet − *Institut des Molécules et Matériaux du Mans (IMMM), UMR 6283 CNRS, Le Mans Université, 72085 Le Mans Cedex 9, France*; orcid.org/0000-0001-7590-1119; Email: amandine.guiet@univ-lemans.fr

Authors

Zahra Goharibajestani − *Institut des Molécules et Matériaux du Mans (IMMM), UMR 6283 CNRS, Le Mans Université, 72085 Le Mans Cedex 9, France*

Yawen Wang − *Institut de Chimie des Milieux et Matériaux de Poitiers (IC2MP), UMR 7285 CNRS, Université de Poitiers, 86073 Poitiers Cedex 9, France*

Valentine Camus-Genot − *Institut des Molécules et Matériaux du Mans (IMMM), UMR 6283 CNRS, Le Mans Université, 72085 Le Mans Cedex 9, France*

Sandrine Arrii − *Institut de Chimie des Milieux et Matériaux de Poitiers (IC2MP), UMR 7285 CNRS, Université de Poitiers, 86073 Poitiers Cedex 9, France*

Jean Dominique Comparot − *Institut de Chimie des Milieux et Matériaux de Poitiers (IC2MP), UMR 7285 CNRS, Université de Poitiers, 86073 Poitiers Cedex 9, France*

Baptiste Polteau − *Institut des Molécules et Matériaux du Mans (IMMM), UMR 6283 CNRS, Le Mans Université, 72085 Le Mans Cedex 9, France*

Jérôme Lhoste − *Institut des Molécules et Matériaux du Mans (IMMM), UMR 6283 CNRS, Le Mans Université, 72085 Le Mans Cedex 9, France*; orcid.org/0000-0002-4570-6459

Cyrille Galven − *Institut des Molécules et Matériaux du Mans (IMMM), UMR 6283 CNRS, Le Mans Université, 72085 Le Mans Cedex 9, France*

Veyis Gunes − *Institut des Molécules et Matériaux du Mans (IMMM), UMR 6283 CNRS, Le Mans Université, 72085 Le Mans Cedex 9, France*

Annie Hémon-Ribaud − *Institut des Molécules et Matériaux du Mans (IMMM), UMR 6283 CNRS, Le Mans Université, 72085 Le Mans Cedex 9, France*; orcid.org/0000-0003-4845-5971

Sagrario Pascual − *Institut des Molécules et Matériaux du Mans (IMMM), UMR 6283 CNRS, Le Mans Université, 72085 Le Mans Cedex 9, France*; orcid.org/0000-0002-9890-0095

Monique Body − *Institut des Molécules et Matériaux du Mans (IMMM), UMR 6283 CNRS, Le Mans Université, 72085 Le Mans Cedex 9, France*

Christophe Legein − *Institut des Molécules et Matériaux du Mans (IMMM), UMR 6283 CNRS, Le Mans Université, 72085 Le Mans Cedex 9, France*; orcid.org/0000-0001-7426-8817

Vincent Maisonneuve − *Institut des Molécules et Matériaux du Mans (IMMM), UMR 6283 CNRS, Le Mans Université, 72085 Le Mans Cedex 9, France*; orcid.org/0000-0003-0570-953X

Complete contact information is available at: https://pubs.acs.org/10.1021/acsanm.1c01768

Notes

The authors declare no competing financial interest.

■ ACKNOWLEDGMENTS

Y.W. thanks the University of Poitiers for her PhD grant. The authors wish to thank Dr François Metz and Dr Eric Perin from Solvay (St Fons, France) for their fruitful discussions. The authors greatly acknowledge the platforms "Diffusion et Diffraction des rayons X" and "Electronic Microscopy" of IMMM. Thanks are also due to the Université Bretagne Loire and University of Le Mans for the postdoctoral grant of Z. G. and the Fondation Banque Polulaire d'Entreprise de l'Ouest for financial support.

■ REFERENCES

(1) Stein, A.; Wilson, B. E.; Rudisill, S. G. Design and Functionality of Colloidal−Crystal−Templated Materials—Chemical Applications of Inverse Opals. *Chem. Soc. Rev.* **2013**, *42*, 2763−2803.

(2) Yamashita, H.; Mori, K.; Kuwahara, Y.; Kamegawa, T.; Wen, M.; Verma, P.; Che, M. Single-Site and Nano-Confined Photocatalysts Designed in Porous Materials for Environmental Uses and Solar Fuels. *Chem. Soc. Rev.* **2018**, *47*, 8072−8096.

(3) Gu, D.; Schüth, F. Synthesis of Non-Siliceous Mesoporous Oxides. *Chem. Soc. Rev.* **2014**, *43*, 313−344.

(4) Kresge, C. T.; Leonowicz, M. E.; Roth, W. J.; Vartuli, J. C.; Beck, J. S. Ordered Mesoporous Molecular Sieves Synthesized by a Liquid-Crystal Template Mechanism. *Nature* **1992**, *359*, 710−712.
(5) Shi, Y.; Wan, Y.; Zhao, D. Ordered Mesoporous Non-Oxide Materials. *Chem. Soc. Rev.* **2011**, *40*, 3854−3878.
(6) Pal, N.; Bhaumik, A. Soft Templating Strategies for the Synthesis of Mesoporous Materials: Inorganic, Organic-Inorganic Hybrid and Purely Organic Solids. *Adv. Colloid Interface Sci.* **2013**, *189*−*190*, 21−41.
(7) Deng, X.; Chen, K.; Tüysüz, H. Protocol for the Nanocasting Method: Preparation of Ordered Mesoporous Metal Oxides. *Chem. Mater.* **2017**, *29*, 40−52.
(8) Mao, Y.; Zhang, F.; Wong, S. S. Ambient Template-Directed Synthesis of Single-Crystalline Alkaline-Earth Metal Fluoride Nanowires. *Adv. Mater.* **2006**, *18*, 1895−1899.
(9) Zhang, F.; Wan, Y.; Shi, Y.; Tu, B.; Zhao, D. Ordered Mesostructured Rare-Earth Fluoride Nanowire Arrays with Upconversion Fluorescence. *Chem. Mater.* **2008**, *20*, 3778−3784.
(10) Zhang, F.; Zhao, D. Fabrication of Ordered Magnetite-Doped Rare Earth Fluoride Nanotube Arrays by Nanocrystal Self-Assembly. *Nano Res.* **2009**, *2*, 292−305.
(11) Wang, Y.; Gohari Bajestani, Z.; Lhoste, J.; Auguste, S.; Hémon-Ribaud, A.; Body, M.; Legein, C.; Maisonneuve, V.; Guiet, A.; Brunet, S.; Gohari Bajestani, Z.; Lhoste, J.; Auguste, S.; Hemon-Ribaud, A.; Body, M.; Legein, C.; Maisonneuve, V.; Guiet, A.; Brunet, S. The Effects of Various Parameters of the Microwave-Assisted Solvothermal Synthesis on the Specific Surface Area and Catalytic Performance of MgF_2 Nanoparticles. *Materials* **2020**, *13*, 3566.
(12) Astruc, A.; Cochon, C.; Dessources, S.; Célérier, S.; Brunet, S. High Specific Surface Area Metal Fluorides as Catalysts for the Fluorination of 2-Chloropyridine by HF. *Appl. Catal. A Gen.* **2013**, *453*, 20−27.
(13) Mao, W.; Jia, Z.; Bai, Y.; Qin, Y.; Wang, B.; Han, S.; Zhang, W.; Kou, L.; Lu, J.; Kemnitz, E. Fe/Hollow Nano-MgF_2: A Green and Highly-Efficient Alternative to Classical Cr-Based Catalysts for the Gas-Phase Fluorination Reaction. *Catal. Sci. Technol.* **2019**, *9*, 3015−3019.
(14) Kemnitz, E. Nanoscale Metal Fluorides: A New Class of Heterogeneous Catalysts. *Catal. Sci. Technol.* **2015**, *5*, 786−806.
(15) Lennon, D.; Winfield, J. M. Metal Fluorides, Metal Chlorides and Halogenated Metal Oxides as Lewis Acidic Heterogeneous Catalysts. Providing Some Context for Nanostructured Metal Fluorides. *Molecules* **2017**, *22*, 201.
(16) Leblanc, M.; Maisonneuve, V.; Tressaud, A. Crystal Chemistry and Selected Physical Properties of Inorganic Fluorides and Oxide-Fluorides. *Chem. Rev.* **2015**, *115*, 1191−1254.
(17) Raut, H. K.; Dinachali, S. S.; Ansah-Antwi, K. K.; Anand Ganesh, V.; Ramakrishna, S. Fabrication of Highly Uniform and Porous MgF_2 Anti-Reflective Coatings by Polymer-Based Sol−Gel Processing on Large-Area Glass Substrates. *Nanotechnology* **2013**, *24*, 505201−505209.
(18) Bernsmeier, D.; Polte, J.; Ortel, E.; Krahl, T.; Kemnitz, E.; Kraehnert, R. Antireflective Coatings with Adjustable Refractive Index and Porosity Synthesized by Micelle-Templated Deposition of MgF_2 Sol Particles. *ACS Appl. Mater. Interfaces* **2014**, *6*, 19559−19565.
(19) Zhang, F.; Deng, Y.; Shi, Y.; Zhang, R.; Zhao, D. Photoluminescence Modification in Upconversion Rare-Earth Fluoride Nanocrystal Array Constructed Photonic Crystals. *J. Mater. Chem.* **2010**, *20*, 3895−3900.
(20) Yang, Y.; Zhou, P.; Xu, W.; Xu, S.; Jiang, Y.; Chen, X.; Song, H. $NaYF_4$:Yb^{3+},Tm^{3+} Inverse Opal Photonic Crystals and $NaYF_4$:Yb^{3+},Tm^{3+}/TiO_2 Composites: Synthesis, Highly Improved Upconversion Properties and NIR Photoelectric Response. *J. Mater. Chem. C* **2016**, *4*, 659−662.
(21) Li, Z.-X.; Li, L.-L.; Zhou, H.-P.; Yuan, Q.; Chen, C.; Sun, L.-D.; Yan, C.-H. Colour Modification Action of an Upconversion Photonic Crystal. *Chem. Commun.* **2009**, *43*, 6616−6618.
(22) Noack, J.; Teinz, K.; Schaumberg, C.; Fritz, C.; Rüdiger, S.; Kemnitz, E. Metal Fluoride Materials with Complex Pore Structure and Organic Functionality. *J. Mater. Chem.* **2011**, *21*, 334−338.
(23) Tao, L.; Xu, W.; Zhu, Y.; Xu, L.; Zhu, H.; Liu, Y.; Xu, S.; Zhou, P.; Song, H. Modulation of Upconversion Luminescence in Er^{3+}, Yb^{3+}-Codoped Lanthanide Oxyfluoride (YOF, GdOF, LaOF) Inverse Opals. *J. Mater. Chem. C* **2014**, *2*, 4186−4195.
(24) Rüdiger, S.; Groß, U.; Kemnitz, E. Non-Aqueous Sol-Gel Synthesis of Nano-Structured Metal Fluorides. *J. Fluor. Chem.* **2007**, *128*, 353−368.
(25) Rao, J. P.; Geckeler, K. E. Polymer Nanoparticles: Preparation Techniques and Size-Control Parameters. *Prog. Polym. Sci.* **2011**, *36*, 887−913 Elsevier Ltd July.
(26) Kemnitz, E.; Wuttke, S.; Coman, S. M. Tailor-Made MgF_2 Based Catalysts by Sol-Gel Synthesis. *Eur. J. Inorg. Chem.* **2011**, 4773−4794 John Wiley & Sons, Ltd November 1.
(27) Teinz, K.; Wuttke, S.; Börno, F.; Eicher, J.; Kemnitz, E. Highly Selective Metal Fluoride Catalysts for the Dehydrohalogenation of 3-Chloro-1,1,1,3-Tetrafluorobutane. *J. Catal.* **2011**, *282*, 175−182.
(28) Krishna Murthy, J.; Gross, U.; Rüdiger, S.; Kemnitz, E. FeF_3/MgF_2: Novel Lewis Acidic Catalyst Systems. *Appl. Catal. A Gen.* **2004**, *278*, 133−138.
(29) Frouri, F.; Célérier, S.; Ayrault, P.; Richard, F. Inorganic Hydroxide Fluorides as Solid Catalysts for Acylation of 2-Methylfuran by Acetic Anhydride. *Appl. Catal. B Environ.* **2015**, *168*−*169*, 515−523.
(30) Troncea, S. B.; Wuttke, S.; Kemnitz, E.; Coman, S. M.; Parvulescu, V. I. Hydroxylated Magnesium Fluorides as Environmentally Friendly Catalysts for Glycerol Acetylation. *Appl. Catal. B Environ.* **2011**, *107*, 260−267.
(31) Agirrezabal-Telleria, I.; Hemmann, F.; Jäger, C.; Arias, P. L.; Kemnitz, E. Functionalized Partially Hydroxylated MgF_2 as Catalysts for the Dehydration of d-Xylose to Furfural. *J. Catal.* **2013**, *305*, 81−91.
(32) Agirrezabal-Telleria, I.; Guo, Y.; Hemmann, F.; Arias, P. L.; Kemnitz, E. Dehydration of Xylose and Glucose to Furan Derivatives Using Bifunctional Partially Hydroxylated MgF_2 Catalysts and N_2-Stripping. *Catal. Sci. Technol.* **2014**, *4*, 1357−1368.
(33) Jia, Z.; Mao, W.; Bai, Y.; Wang, B.; Ma, H.; Li, C.; Lu, J. Hollow Nano- MgF2- Supported Catalysts: Highly Active and Stable in Gas-Phase Dehydro Fl Uorination of 1 , 1 , 1 , 3 , 3-Penta Fl Uoropropane. *Appl. Catal. B Environ.* **2018**, *238*, 599−608.
(34) Camli, S. T.; Buyukserin, F.; Balci, O.; Budak, G. G. Size Controlled Synthesis of Sub-100 Nm Monodisperse Poly-(Methylmethacrylate) Nanoparticles Using Surfactant-Free Emulsion Polymerization. *J. Colloid Interface Sci.* **2010**, *344*, 528−532.
(35) Capek, I. Microemulsion Polymerization of Styrene in the Presence of Anionic Emulsifier. *Adv. Colloid Interface Sci.* **1999**, *82*, 253−273.
(36) Gan, L. M.; Lee, K. C.; Chew, C. H.; Ng, S. C. Effects of Surfactant Concentration on Polymerizations of Methyl Methacrylate and Styrene in Emulsions and Microemulsions. *Langmuir* **1995**, *11*, 449−454.
(37) Waltz, F.; Swider, M. A.; Hoyer, P.; Hassel, T.; Erne, M.; Möhwald, K.; Adlung, M.; Feldhoff, A.; Wickleder, C.; Bach, F.-W.; Behrens, P. Synthesis of Highly Stable Magnesium Fluoride Suspensions and Their Application in the Corrosion Protection of a Magnesium Alloy. *J. Mater. Sci.* **2012**, *47*, 176−183.
(38) Sandi, A.; Sawitri, A.; Rajak, A.; Zulfi, A.; Edikresnha, D.; Munir, M. M.; Khairurrijal, K. Fabrication and Characterization of Monodisperse Polystyrene Latex (PSL) with Various Diameters. *IOP Conf. Ser. Mater. Sci. Eng.* **2018**, *367*, 012015.
(39) Everett, D. H. Manual of Symbols and Terminology for Physicochemical Quantities and Units, Appendix II: Definitions, Terminology and Symbols in Colloid and Surface Chemistry. *Pure Appl. Chem.* **1972**, *31*, 577 Butterworths: London.
(40) Baur, W. H. Rutile-Type Compounds. V. Refinement of MnO_2 and MgF_2. *Acta Crystallogr. Sect. B Struct. Crystallogr. Cryst. Chem.* **1976**, *32*, 2200−2204.

(41) Sadoc, A.; Body, M.; Legein, C.; Biswal, M.; Fayon, F.; Rocquefelte, X.; Boucher, F. NMR Parameters in Alkali, Alkaline Earth and Rare Earth Fluorides from First Principle Calculations. *Phys. Chem. Chem. Phys.* **2011**, *13*, 18539−18550.
(42) Prescott, H. A.; Li, Z.-J.; Kemnitz, E.; Deutsch, J.; Lieske, H. New Magnesium Oxide Fluorides with Hydroxy Groups as Catalysts for Michael Additions. *J. Mater. Chem.* **2005**, *15*, 4616−4628.
(43) Sideris, P. J.; Nielsen, U. G.; Gan, Z.; Grey, C. P. Mg/Al Ordering in Layered Double Hydroxides Revealed by Multinuclear NMR Spectroscopy. *Science* **2008**, *321*, 113−117.
(44) Wuttke, S.; Vimont, A.; Lavalley, J.-C.; Daturi, M.; Kemnitz, E. Infrared Investigation of the Acid and Basic Properties of a Sol−Gel Prepared MgF_2. *J. Phys. Chem. C* **2010**, *114*, 5113−5120.
(45) Astruc, A.; Célérier, S.; Pavon, E.; Mamede, A.-S.; Delevoye, L.; Brunet, S. Mixed $Ba_{1-x}La_xF_{2+x}$ Fluoride Materials as Catalyst for the Gas Phase Fluorination of 2-Chloropyridine by HF. *Appl. Catal. B Environ.* **2017**, *204*, 107−118.
(46) Le Bail, A.; Duroy, H.; Fourquet, J. L. Ab-Initio Structure Determination of $LiSbWO_6$ by X-Ray Powder Diffraction. *Mater. Res. Bull.* **1988**, *23*, 447−452.
(47) Rodríguez-Carvajal, J. Recent Advances in Magnetic Structure Determination by Neutron Powder Diffraction. *Phys. B Phys. Condens. Matter* **1993**, *192*, 55−69.
(48) Thompson, P.; Cox, D. E.; Hastings, J. B. Rietveld Refinement of Debye−Scherrer Synchrotron X-Ray Data from Al_2O_3. *J. Appl. Crystallogr.* **1987**, *20*, 79−83.
(49) Langford, J. I. A Rapid Method for Analysing the Breadths of Diffraction and Spectral Lines Using the Voigt Function. *J. Appl. Crystallogr.* **1978**, *11*, 10−14.
(50) Rasband, W. *ImageJ Software*; National Institutes of Health: Bethesda, MD, available at http://rsb.info.nih.gov/ij.
(51) Rasband, W. *ImageJ Software*; National Institutes of Health: Bethesda.
(52) Massiot, D.; Fayon, F.; Capron, M.; King, I.; Le Calvé, S.; Alonso, B.; Durand, J.-O.; Bujoli, B.; Gan, Z.; Hoatson, G. Modelling One- and Two-Dimensional Solid-State NMR Spectra. *Magn. Reson. Chem.* **2002**, *40*, 70−76.

https://doi.org/10.1021/acsanm.1c01768
ACS Appl. Nano Mater. XXXX, XXX, XXX−XXX